

Inverse design of a spatial demultiplexer for free-space optical communications: direct optimization over turbulence statistics

Nicolas Barré^{1,*}

¹Independent researcher

*email: nicolas.barre@protonmail.com

March 20, 2026

Abstract

Atmospheric turbulence severely limits the coupling of received optical wavefronts into single-mode fibers in satellite-to-ground free-space optical links. Spatial demultiplexing receivers address this challenge by distributing the incoming field across a bundle of single-mode fibers whose outputs are recombined coherently, relaxing the requirements on wavefront correction. In this work, we investigate the design of such receivers from two complementary angles. We first compare the power coupling statistics achieved by several modal bases and show that the spatial support of the modes matters far more than the specific choice of basis, questioning the relevance of mode-selective approaches for this application. We then present the inverse design of a compact two-plane refractive system optimized directly over an ensemble of turbulence realizations using stochastic gradient descent, with no constraint imposed on the input modal decomposition. The optimized system significantly improves over direct coupling into the fiber bundle, approaches the performance of an ideal modal projection, and remains competitive across a broad range of turbulence conditions.

1 Introduction

Free-space optical (FSO) communications offer a promising alternative to radio-frequency links for high-throughput ground-to-satellite and inter-building connectivity [1]. A central challenge in FSO systems is the coupling of the received optical wavefront into single-mode fibers, which is severely degraded by atmospheric turbulence. Turbulence introduces wavefront distortions that reduce the spatial coherence of the received field, leading to coupling losses and signal fading that directly limit the link budget.

Two main strategies have been developed to mitigate this effect. The first relies on adaptive optics, where a wavefront sensor and a deformable mirror correct the incoming wavefront in real time to restore single-mode fiber coupling [2, 3]. The second strategy, which is the focus of this work, relies on spatial demultiplexing: the turbulent wavefront is distributed across a set of single-mode fibers, and the outputs are recombined coherently to recover the transmitted signal [4, 5, 6, 7].

Two main device architectures have been explored to implement this spatial demultiplexing. Photonic lanterns, originally developed for astronomical instrumentation [8], interface a bundle of single-mode fibers with the incoming multimode beam through an adiabatic waveguide taper [9]. Ultrafast laser inscription has since extended this concept to complex three-dimensional geometries [10], improving robustness and design flexibility. Multi-plane light conversion (MPLC), on the other hand, realizes a fully controlled unitary transformation between a prescribed set of orthogonal spatial modes through successive free-space phase modulations [11, 12, 13]. A recent experimental comparison over a simulated GEO-to-ground FSO link has shown that a seven-port photonic lantern achieves on average 1 dB lower coupling losses than a commercial 15-mode MPLC module, at the cost of higher signal fading [7].

The design of multi-element diffractive optical systems, in which a wavefront undergoes successive phase modulations separated by free-space propagation, has a long history predating the optical neural network literature. As early as 1993, Fienup established gradient-based inverse design of cascaded phase elements as a viable computational approach [14]. Wang and Piestun later applied equivalent functionality using cascaded planar elements optimized through iterative projection algorithms, in the context of volumetric holography and multicolor beam shaping [15]. Independently, the optical neural network community framed the same physical architecture as an end-to-end differentiable computing substrate, optimized for arbitrary objective functions [16, 17, 18, 19]. Within this framework, MPLC can be viewed as a particular instantiation that uses phase masks as optical elements and restricts the transformation to a unitary mapping between a fixed set of orthogonal input and output spatial modes, a natural choice for telecommunications where mode orthogonality defines the independent channels that carry information. The approach presented here is fundamentally different: no input modal basis is defined, and no orthogonal mode decomposition is imposed. Instead, the optimization criterion is directly the total power collected into the single-mode fibers, averaged over an ensemble of atmospheric turbulence realizations, which is the physical quantity of interest in free-space optical communications.

In this work, we approach the design of FSO spatial demultiplexers from two complementary angles. We first systematically compare the power coupling distributions achieved by several modal bases for turbulent wavefront collection, and show that the choice of detection basis has a limited impact on power collection efficiency, provided the spatial support of the modes covers the collecting pupil efficiently. We then present the inverse design of a compact two-plane refractive system optimized directly over an ensemble of atmospheric turbulence realizations using stochastic gradient descent, without any constraint on the input modal decomposition. The optimized system approaches the performance of an ideal Karhunen-Loève modal projection and significantly improves over direct coupling into the fiber bundle, while remaining competitive across a broad range of turbulence conditions.

2 Modal basis comparison for turbulent wavefront power coupling

The fraction of power that can be collected from a turbulent wavefront depends on the choice of modal basis onto which the incoming field is projected. Before designing any physical system, it is therefore instructive to compare the power coupling distributions achieved by different modal bases, independently of any hardware constraint. This section establishes the theoretical upper bound set by the Karhunen-Loève basis, introduces the statistical characterization methodology used throughout this work, and compares the performance of several practically relevant modal bases.

2.1 Turbulence statistics and Karhunen-Loève basis

Atmospheric turbulence is modeled using a modified Von Kármán power spectrum as defined in [20]:

$$\Phi_\phi(u) = 0.0299 \cdot r_0^{-5/3} \cdot \frac{\exp(-u^2/u_o^2)}{(u^2 + u_i^2)^{11/6}}, \quad (1)$$

where Φ_ϕ is the two-dimensional power spectral density of the wavefront phase, u is the spatial frequency in cycles per meter, r_0 is the Fried parameter, and $u_i = 1/l_0$ and $u_o = 1/L_0$ are the spatial frequencies associated with the inner scale l_0 and outer scale L_0 , respectively.

In practice, FSO receivers operate with collecting apertures ranging from a few centimeters to tens of centimeters. Rather than simulating at the physical scale of the receiver, we work in a reduced coordinate system where the pupil diameter is set to $D = 160 \mu\text{m}$, corresponding to the assumption that a telescope images the collecting aperture onto the input of the demultiplexer. All results depend only on the dimensionless ratio D/r_0 , which fully characterizes the turbulence strength relative to the aperture size, and are therefore independent of the physical scale of the simulation.

Phase screens are generated on a 300×300 grid with sampling $\Delta x = 1 \mu\text{m}$, giving a simulation domain of $300 \mu\text{m}$, slightly larger than the pupil to avoid Fourier artifacts at the pupil boundary. The inner scale is set by the grid sampling, $l_0 = \Delta x = 1 \mu\text{m}$. To extend the outer scale and suppress low-frequency artifacts inherent

to FFT-based generation, the grid is zero-padded by a factor of 8 prior to spectral filtering, giving an effective outer scale $L_0 = 8 \times 300 \mu\text{m} = 2400 \mu\text{m}$. A set of $N = 3000$ independent turbulent phase screens is generated at $D/r_0 = 8$, corresponding to moderate turbulence conditions representative of a ground-to-satellite FSO link.

To identify the optimal modal basis for power coupling, we arrange the $N = 3000$ turbulent wavefront realizations as columns of a data matrix $X \in \mathbb{R}^{N_{\text{pix}} \times N}$ with $N_{\text{pix}} = 300 \times 300$, where each realization is masked by the circular collecting pupil prior to vectorization. The left singular vectors of X , obtained by singular value decomposition, form the Karhunen-Loève (KL) basis adapted to the turbulence statistics. Fig. 1 shows the normalized power spectrum of the generated phase screens alongside representative turbulent wavefront realizations at $D/r_0 = 8$, confirming that the simulated turbulence follows the expected Von Kármán statistics.

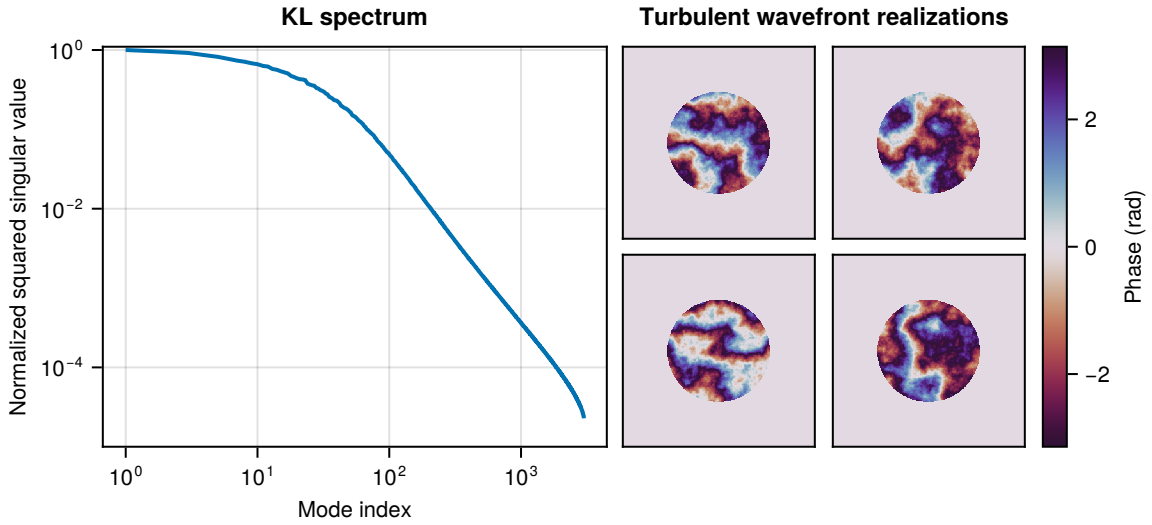


Fig. 1: Left: normalized squared singular value spectrum of the Karhunen-Loève basis, showing the rapid decay of the eigenvalues. Right: four representative turbulent wavefront realizations at $D/r_0 = 8$, displayed within the circular collecting pupil. The phase is shown in radians.

By construction, this basis maximizes the power captured by a truncated set of modes and serves as the theoretical upper bound for any fixed modal decomposition. We retain the first 91 KL modes, which capture the dominant fraction of the turbulent wavefront energy for the considered D/r_0 range. For each turbulent realization, we compute the total power fraction $\eta \in [0, 1]$ collected into the 91 KL modes. Fig. 2 shows the resulting time series of η over 300 representative realizations, as well as the full distribution over the 3000 realizations, both without and with tip-tilt correction applied to the incoming wavefront prior to projection. Tip-tilt correction is considered here as a practically relevant pre-processing step, as fast tip-tilt mirrors are routinely deployed in FSO systems to compensate beam wander at low cost and without the complexity of full adaptive optics correction. The distribution is well described by a Kumaraswamy distribution, a flexible two-parameter model for bounded random variables whose asymmetric shape, with a tail toward low values, is better suited to the observed coupling statistics than a symmetric model such as the Beta distribution. Its probability density function reads

$$f(\eta; a, b) = ab\eta^{a-1}(1-\eta^a)^{b-1}, \quad \eta \in [0, 1], \quad (2)$$

allowing the mean coupling efficiency and fading statistics to be characterized by just two parameters. This fitting methodology is used consistently for all modal bases considered in this work. Tip-tilt correction provides a modest improvement in mean coupling efficiency ($\bar{\eta} = 0.850$ without correction, $\bar{\eta} = 0.880$ with correction), but significantly reduces the standard deviation of the coupling fluctuations ($\sigma = 0.033$ without, $\sigma = 0.015$ with), thereby mitigating fading events by a factor of approximately two in standard deviation.

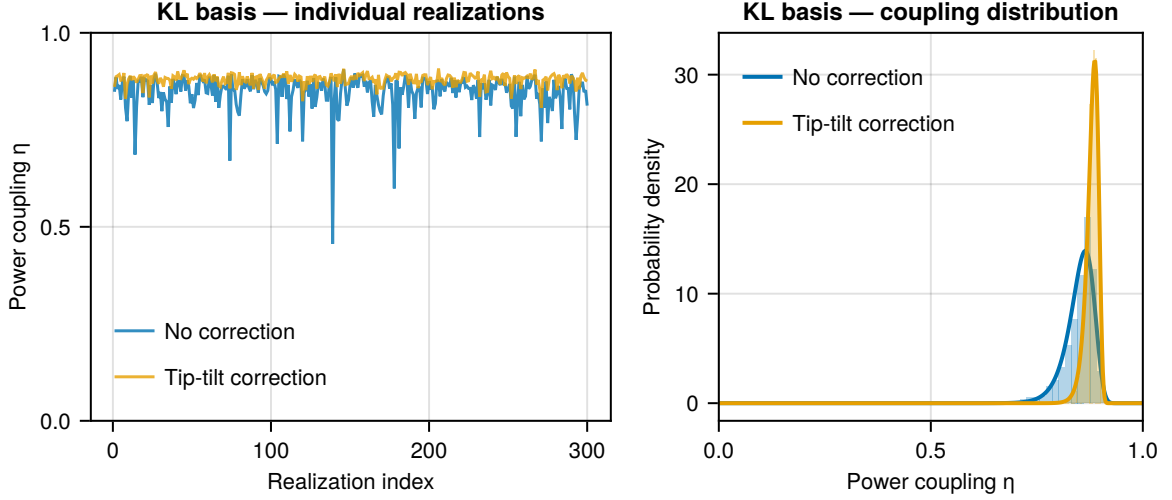


Fig. 2: Power coupling efficiency η of the Karhunen-Loève basis at $D/r_0 = 8$, without (blue) and with (orange) tip-tilt correction. Left: η over 300 representative turbulent realizations. Right: distribution of η over 3000 realizations, with fitted Kumaraswamy distributions overlaid.

2.2 Alternative modal bases and power coupling distributions

We define three additional modal bases and evaluate their power coupling distributions using the same methodology. The first is a 91-mode Laguerre-Gaussian (LG) basis, with waist parameter $w_{LG} = 24.5 \mu\text{m}$ optimized to maximize the mean power coupling over the turbulence ensemble. This basis is a standard reference in spatial division multiplexing and represents a natural fixed analytical choice requiring no prior knowledge of the turbulence statistics. The second and third bases share a common concentric ring layout: modes are arranged in a central spot surrounded by 6 concentric rings, each ring containing 4 more equally-spaced spots than the preceding ring, starting with 5 spots on the innermost ring, for a total of 91 modes including the central spot. In the wide packing variant, modes have waist $w_G = 4.2 \mu\text{m}$ with a center-to-center separation of $3w_G$, ensuring approximate orthogonality of the individual modes. In the dense packing variant, the waist is increased to $w'_G = 11.5 \mu\text{m}$ with a center-to-center separation of w'_G , resulting in a strongly non-orthogonal set that is subsequently re-orthonormalized using a Gram-Schmidt procedure. The total intensity summed over the 91 modes of each basis is shown in Fig. 3, confirming that all four bases provide good spatial coverage of the collecting pupil.

The power coupling distributions for all four bases, fitted with Kumaraswamy distributions, are shown in Fig. 4 and summarized in Table 1, for both the uncorrected and tip-tilt corrected cases. The KL basis achieves the highest mean coupling efficiency by construction, reaching $\bar{\eta} = 0.850$ without correction and $\bar{\eta} = 0.880$ with tip-tilt correction. The LG basis and the dense packing basis perform comparably, with mean efficiencies within 1.5% of each other in both cases and a slight advantage for dense packing. To further characterize the relationship between these bases, we compute their pairwise power coupling overlap, defined as

$$O(u, v) = \frac{1}{N} \sum_{i,j} |\langle u_i | v_j \rangle|^2, \quad (3)$$

where $\{u_i\}$ and $\{v_j\}$ are two orthonormal bases of N modes. This quantity equals 1 when the two bases span the same subspace and measures the fraction of power transferable between them. The resulting overlap matrix is given in Table 2. Both the LG and dense packing bases recover approximately 80% of the KL subspace, consistently with their similar mean coupling efficiencies. Their mutual overlap of 86% further indicates that

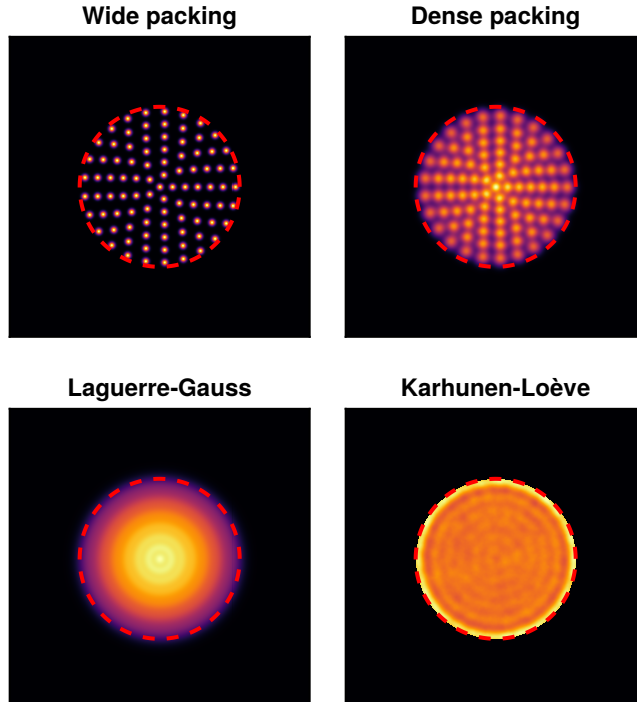


Fig. 3: Total intensity of the four modal bases considered in this work, summed over the first 91 modes: wide packing (top left), dense packing (top right), Laguerre-Gauss (bottom left), and Karhunen-Loève (bottom right). The dashed red circle indicates the boundary of the collecting pupil of diameter $D = 160 \mu\text{m}$.

despite their near-equivalent performance, they do not span exactly the same functional space and collect partly different turbulence modes. The dense packing basis, re-orthonormalized from a set of overlapping Gaussians, spans a similar functional space to that of fs-laser written photonic lanterns, where closely-spaced fiber cores merge in the tapered section. In both cases the individual mode shapes are not precisely controlled, yet the near-equivalence with LG performance confirms that what matters is that the spatial span of the basis covers the collecting pupil efficiently, rather than the precise shape of its individual modes.

Table 1: Mean power coupling efficiency $\bar{\eta}$ and standard deviation σ for the four modal bases, without and with tip-tilt correction, at $D/r_0 = 8$.

Basis	No correction		Tip-tilt corrected	
	$\bar{\eta}$	σ	$\bar{\eta}$	σ
Karhunen-Loève	0.850	0.033	0.880	0.015
Laguerre-Gauss	0.786	0.038	0.818	0.020
Wide packing	0.390	0.019	0.408	0.011
Dense packing	0.796	0.039	0.830	0.019

The wide packing basis, where fiber modes do not overlap, represents the performance achievable with a simple fiber bundle and a microlens array requiring no optical optimization, and reaches only $\bar{\eta} \approx 0.39$, a factor of two below the other bases. Interestingly, it also exhibits the lowest coupling standard deviation ($\sigma = 0.019$ without correction), as the spatial diversity of non-overlapping modes averages out turbulence fluctuations at the cost of reduced mean efficiency. This is the operating principle of multi-aperture receivers, here quantified in direct comparison with modal bases of comparable complexity. Tip-tilt correction provides a modest but

Table 2: Pairwise power coupling overlap $O(u, v)$ as defined in Eq. 3 between the Karhunen-Loève, Laguerre-Gauss, and dense packing bases.

	KL	LG	Dense packing
KL	1.000	0.790	0.806
LG	0.790	1.000	0.861
Dense packing	0.806	0.861	1.000

consistent improvement in mean coupling efficiency across all bases (+3 to +5 percentage points), while more significantly reducing the standard deviation of the coupling fluctuations by approximately a factor of two, which is practically relevant for FSO link reliability. These results motivate the inverse design approach developed in the following section, where the output mode arrangement is no longer constrained to any predefined basis and power coupling over turbulence statistics is maximized directly.

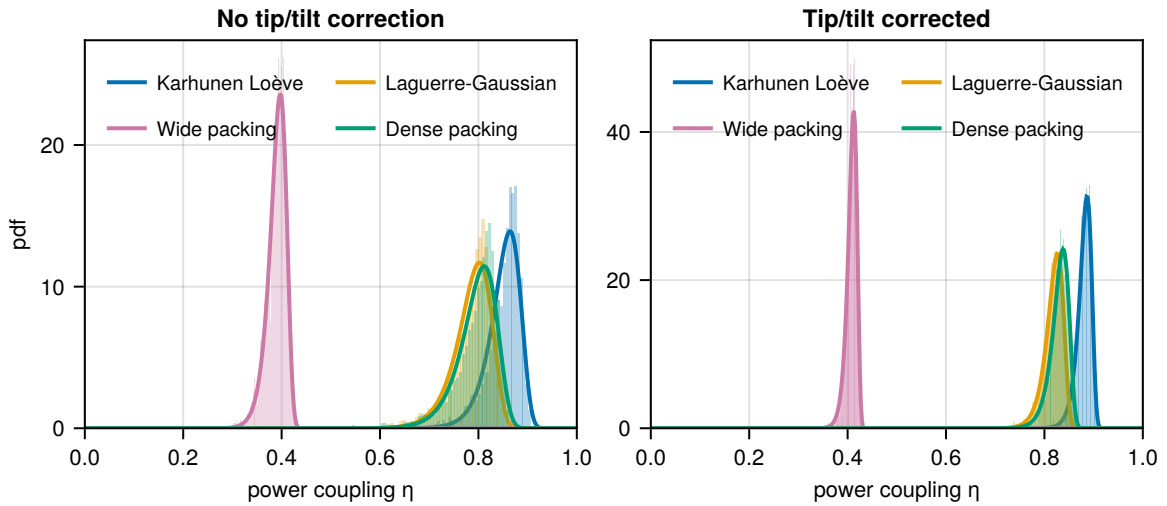


Fig. 4: Power coupling efficiency distributions for the four modal bases considered in this work at $D/r_0 = 8$. Left: without tip-tilt correction. Right: with tip-tilt correction. Histograms show the empirical distributions over 3000 turbulent realizations; solid curves show the fitted Kumaraswamy distributions.

3 Inverse design of a two-plane free-space to fiber bundle demultiplexer

The previous section established that the choice of modal basis has a limited impact on power coupling efficiency, provided the spatial support of the modes is well matched to the collecting pupil. This motivates a different question: given a fixed physical architecture, can direct optimization over turbulence statistics yield a system that approaches the theoretical upper bound set by the Karhunen-Loève basis, without any reference to an input modal decomposition?

3.1 Optical system description

We consider a compact two-plane refractive system depicted in Fig. 5, consisting of a single glass slab of refractive index $n = 1.5$ and thickness $150 \mu\text{m}$, whose two end facets are assumed to be freeform surfaces. The input

wavefront, corresponding to the image of the collecting pupil of diameter $160\ \mu\text{m}$, is placed $50\ \mu\text{m}$ before the first freeform surface. In practice, this requires a telescope to image the physical collecting pupil, typically several tens of centimeters to over one meter in diameter, onto the $160\ \mu\text{m}$ input aperture of the device. The output single-mode fiber bundle is placed $50\ \mu\text{m}$ after the second freeform surface, and its geometry corresponds to the 91-mode wide packing with concentric rings described in the previous section. The working wavelength is $\lambda = 1.55\ \mu\text{m}$.

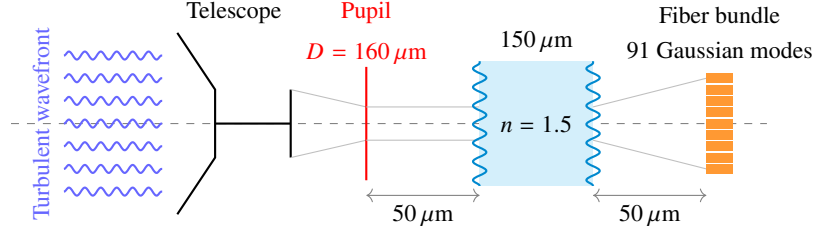


Fig. 5: Schematic of the two-plane refractive demultiplexer. A telescope images the collecting aperture onto a $160\ \mu\text{m}$ input pupil. The optimized glass slab ($n = 1.5$, thickness $150\ \mu\text{m}$) with two freeform surfaces redirects the incoming turbulent wavefront onto an array of 91 single-mode fibers placed $50\ \mu\text{m}$ after the second surface.

3.2 Optimized surfaces and physical interpretation

The freeform surfaces are discretized on a 300×300 grid with sampling $\Delta x = 1\ \mu\text{m}$, as defined in the previous section, and optimized by stochastic gradient descent on the loss function

$$\mathcal{L} = 1 - \mathbb{E}_j \left[\frac{1}{M} \sum_{i=1}^M |\langle u_i | \psi_j \rangle|^2 \right], \quad (4)$$

where $\{u_i\}_{i=1}^M$ are the $M = 91$ fiber bundle modes and ψ_j is a turbulent wavefront drawn from the ensemble of $N = 3000$ realizations generated in the previous section at $D/r_0 = 8$. End-to-end optimization of the surface profiles is performed using FluxOptics.jl [21], an open-source Julia package for differentiable wave optics. At each iteration, the expectation in Eq. (4) is estimated over a batch of $N_b = 300$ randomly drawn realizations from the ensemble:

$$\hat{\mathcal{L}} = 1 - \frac{1}{MN_b} \sum_{i=1}^M \sum_{j=1}^{N_b} |\langle u_i | \psi_j \rangle|^2. \quad (5)$$

This loss function extends the multimode power coupling metric introduced in [22] to the case where the input fields $\{\psi_j\}$ form a statistical ensemble of turbulent wavefront realizations rather than an orthonormal basis, and where $N_b \neq M$.

Optimization runs for 500 iterations, each processing a new batch, and converges in 22 seconds on a GPU GeForce RTX 4070 Super. The resulting phase patterns, shown in Fig. 6, are remarkably smooth and slowly varying, a non-trivial outcome given that the optimization was driven exclusively by random turbulent inputs with no regularity constraint imposed on the surfaces. This smoothness reflects the geometry of the output fiber bundle: the optimization naturally produces a phase profile that locally redirects the incoming wavefront toward each fiber core, in a manner reminiscent of a custom microlens arrangement.

To gain further insight into the optimized system, we back-propagate each Gaussian mode of the fiber bundle through the device and examine the resulting field distribution at the input pupil plane. As shown in Fig. 7, the back-propagated modes form a dense arrangement of deformed Gaussian spots that collectively tile the collecting pupil, strikingly similar to the dense packing basis of the previous section. This spontaneous convergence toward a dense spatial coverage confirms the spatial support maximization principle identified earlier: the optimization

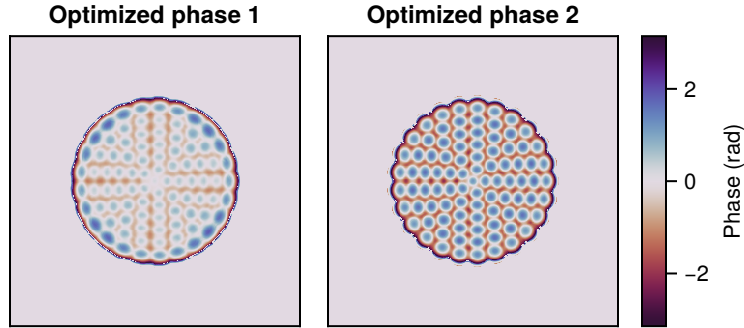


Fig. 6: Optimized phase patterns of the two freeform surfaces of the glass slab. The smooth, slowly-varying structure emerges spontaneously from the optimization on random turbulent inputs, reflecting the geometry of the output fiber bundle. Both panels span $300\ \mu\text{m} \times 300\ \mu\text{m}$.

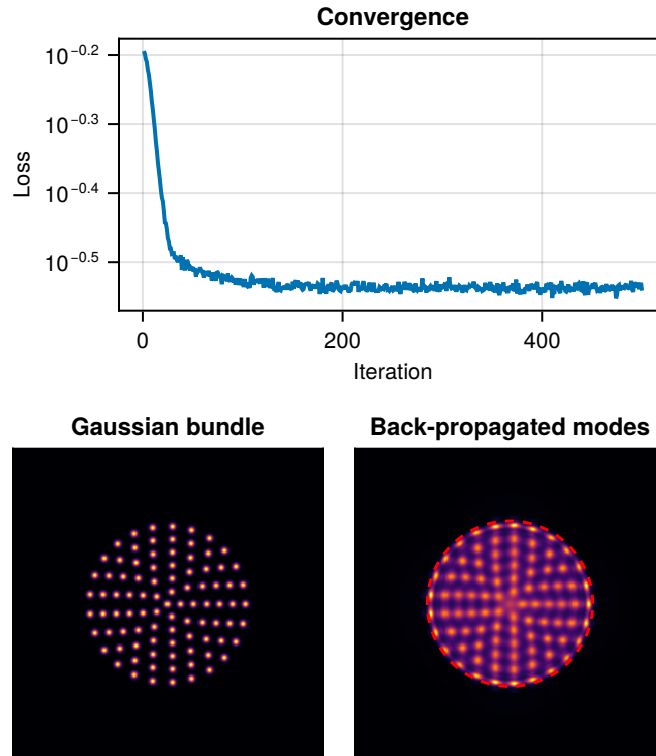


Fig. 7: Top: convergence of the loss function over 500 SGD iterations. Bottom left: total intensity of the Gaussian fiber bundle in the output plane. Bottom right: total intensity of the Gaussian bundle modes back-propagated through the optimized device to the input pupil plane. The dashed red circle indicates the boundary the collecting pupil of diameter $D = 160\ \mu\text{m}$.

has redistributed the input sensitivity of each fiber to cover the pupil as efficiently as possible, without any explicit instruction to do so.

Table 3 summarizes the coupling performance of the optimized system at $D/r_0 = 8$. With a mean coupling efficiency of $\bar{\eta} = 0.713$ without tip-tilt correction and $\bar{\eta} = 0.764$ with correction, the two-plane system lies between the wide packing baseline and the LG and dense packing bases reported in Table 1. This result is consistent with the output Gaussian bundle geometry, which corresponds to the wide packing layout and therefore starts from a less favorable spatial coverage than the dense packing. Tip-tilt correction reduces the coupling standard deviation from $\sigma = 0.053$ to $\sigma = 0.030$, following the same trend observed for the modal bases in the previous section.

Table 3: Mean power coupling efficiency $\bar{\eta}$ and standard deviation σ for the optimized two-plane system, without and with tip-tilt correction, at $D/r_0 = 8$. This data extends Table 1.

	No correction		Tip-tilt corrected	
	$\bar{\eta}$	σ	$\bar{\eta}$	σ
2-plane system	0.713	0.053	0.764	0.030

3.3 Robustness of the optimized design across turbulence regimes

The system was optimized at $D/r_0 = 8$ using a fixed ensemble of $N = 3000$ turbulent realizations. Figure 8 shows the mean coupling efficiency and its standard deviation as a function of $D/r_0 \in [2, 20]$, compared to the KL upper bound, the LG basis projection, and direct fiber coupling, both without and with tip-tilt correction.

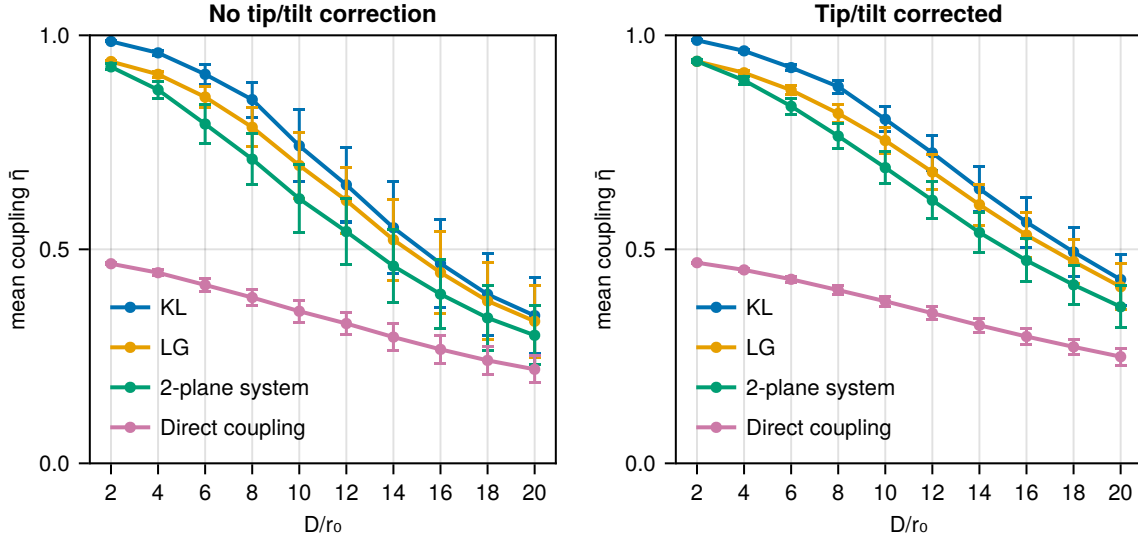


Fig. 8: Mean power coupling efficiency $\bar{\eta}$ as a function of turbulence strength D/r_0 for the KL basis, LG basis, optimized two-plane system, and direct fiber coupling, without (left) and with (right) tip-tilt correction. The two-plane system is optimized at $D/r_0 = 8$. Error bars indicate one standard deviation over the turbulence ensemble.

The two-plane system remains competitive across the full range of turbulence conditions considered. Without tip-tilt correction, the gap between the two-plane system and the KL upper bound increases from 6% at $D/r_0 = 2$ to approximately 17% around $D/r_0 = 10$ –12, before slightly decreasing at higher turbulence strengths as all

bases become limited by the finite number of collected modes. The gap with respect to the ideal LG projection follows a similar trend, ranging from 1.4% at $D/r_0 = 2$ to 12% at $D/r_0 = 12$. Tip-tilt correction substantially improves the relative performance of the two-plane system, particularly at low turbulence strengths. At $D/r_0 = 2$, the corrected two-plane system matches the LG projection to within 0.1%, effectively closing the gap. At the design point $D/r_0 = 8$, the gap with KL is reduced from 16.6% to 13.2%, and the gap with LG from 9.8% to 6.6%. For strong turbulence ($D/r_0 > 12$), the benefit of tip-tilt correction diminishes, as higher-order wavefront aberrations increasingly dominate over beam wander and cannot be compensated by tip-tilt alone. Overall, tip-tilt correction offers a favorable trade-off in the moderate turbulence regime, where it brings the two-plane system close to the performance of an ideal modal projection at minimal added hardware complexity.

A notable observation concerns the coupling variance. Direct fiber coupling, despite its low mean efficiency, exhibits a significantly lower standard deviation than all optimized bases across the entire turbulence range, particularly at high D/r_0 . This is a manifestation of the spatial diversity effect: non-overlapping fiber modes sample independent regions of the pupil and average out turbulence fluctuations, at the cost of reduced mean power collection. Conversely, the KL basis, while optimal in mean, exhibits the highest variance under strong turbulence, as its modes are concentrated in the regions of highest average energy and therefore most sensitive to turbulent fluctuations. The two-plane system occupies an intermediate position, with a variance comparable to the LG basis.

These results suggest that mean coupling efficiency and coupling variance are competing objectives under strong turbulence, and that the current design, optimized solely for mean power, leaves room for improvement in fading statistics. A natural extension would be to include a variance penalty term in the loss function [23], which could further reduce fading without sacrificing mean efficiency.

It is worth noting that the two-plane architecture imposes no constraint on the fiber bundle geometry: the optimizer freely adapts to any spatial arrangement of output modes, whether concentric rings as used here, Cartesian grids, or arbitrary configurations dictated by fabrication constraints. The concentric ring layout was chosen for its circular symmetry and to match the number of modes of the Laguerre-Gaussian basis, but simulations with Cartesian geometries and non-standard mode counts converge equally well, suggesting that the approach is directly applicable to photonic lanterns or multicore fibers of arbitrary design. From a practical standpoint, the two-plane geometry is already well suited for laboratory implementation with a spatial light modulator, while fs-laser written photonic lanterns with dense core packing represent a promising path toward compact, alignment-free hardware embodiments of the same design principle.

4 Conclusion

We have presented a systematic comparison of modal bases for turbulent wavefront power collection in free-space optical communications, followed by the inverse design of a compact two-plane refractive demultiplexer optimized directly over atmospheric turbulence statistics.

The modal basis comparison reveals that the spatial coverage of the collecting pupil is the primary determinant of power collection efficiency, independently of the specific basis chosen. A dense packing of Gaussian modes, after re-orthonormalization, performs as well as an optimal Laguerre-Gaussian basis, and the functional space it spans is analogous to that of fs-laser written photonic lanterns, where closely-spaced fiber cores produce coupled modes that are not individually controlled yet collectively cover the input aperture. Conversely, a sparse orthogonal arrangement of non-overlapping fiber modes achieves only half the coupling efficiency of denser bases.

The optimized two-plane system, designed without any prescribed modal decomposition of the turbulent wavefront, approaches the performance of an ideal Karhunen-Loève projection and significantly improves over direct fiber coupling. Remarkably, the optimized phase patterns are perfectly smooth and respect the geometry of the output fiber bundle, bearing a strong resemblance to a custom microlens arrangement despite having been optimized exclusively on random turbulent inputs. This demonstrates that constraining the demultiplexer to decompose the incoming field onto a prescribed basis, as in MPLC-based approaches targeting a Hermite-Gaussian decomposition, imposes an unnecessary design burden: a two-plane geometry is sufficient to capture most of the

available gain when the optimization criterion is matched to the turbulence statistics and the spatial support of the collected modes covers the pupil efficiently. Back-propagating the fiber bundle modes through the optimized device shows that each fiber mode is mapped to a compact spot in the pupil plane, collectively tiling the available aperture, confirming the spatial support maximization principle identified in the basis comparison. Tip-tilt correction further narrows the performance gap, particularly in the mild turbulence regime.

A key finding of the robustness analysis is that mean coupling efficiency and coupling variance are competing objectives under strong turbulence. The current design, optimized solely for mean power, exhibits higher fading than direct fiber coupling despite its superior mean efficiency, pointing to a natural extension: incorporating a variance penalty into the loss function [23] to simultaneously improve mean efficiency and reduce fading. From a practical perspective, the two-plane geometry is well suited for laboratory validation with a spatial light modulator, and fs-laser written photonic lanterns with dense core packing represent a particularly promising hardware embodiment of the spatial support maximization principle demonstrated here. Coherent combination of the fiber outputs on a photonic integrated circuit [6] would further complete the receiver chain and enable direct comparison with full system performance metrics.

Funding. This research received no external funding.

Data availability. All simulations were performed using FluxOptics.jl [21], an open-source Julia package for differentiable wave optics. Data and code underlying the results presented in this paper are available from the author upon reasonable request.

AI assistance. The author used an AI language model (Claude, Anthropic) as an assistant during the preparation of this manuscript, for tasks including literature search, LaTeX drafting, and technical discussion. All scientific content, simulations, results, and conclusions were developed independently by the author.

References

- [1] Fernando P. Guiomar, Marco A. Fernandes, José Leonardo Nascimento, Vera Rodrigues, and Paulo P. Monteiro. Coherent free-space optical communications: Opportunities and challenges. *Journal of Lightwave Technology*, 40(10):3173–3186, May 2022. doi:[10.1109/JLT.2022.3164736](https://doi.org/10.1109/JLT.2022.3164736).
- [2] Laurie Paillier, Raphaël Le Bidan, Jean-Marc Conan, Géraldine Artaud, Nicolas Védrenne, and Yves Jaouën. Space-ground coherent optical links: Ground receiver performance with adaptive optics and digital phase-locked loop. *Journal of Lightwave Technology*, 38(20):5716–5727, 2020. doi:[10.1109/JLT.2020.3003561](https://doi.org/10.1109/JLT.2020.3003561).
- [3] Yannik Horst, Bertold Ian Bitachon, Laurenz Kulmer, Jannik Brun, Tobias Blatter, Jean-Marc Conan, Aurélie Montmerle-Bonnefois, Joseph Montri, Béatrice Sorrente, Caroline B. Lim, Nicolas Védrenne, Daniel Matter, Loann Pommarel, Benedikt Baeuerle, and Juerg Leuthold. Tbit/s line-rate satellite feeder links enabled by coherent modulation and full-adaptive optics. *Light: Science & Applications*, 12(1):153, Jun 2023. doi:[10.1038/s41377-023-01201-7](https://doi.org/10.1038/s41377-023-01201-7).
- [4] Antonin Billaud, Fausto Gomez, David Allieux, Nicolas Laurenchet, Pu Jian, Olivier Pinel, and Guillaume Labroille. Optimal coherent beam combining based on multi-plane light conversion for high throughput optical feeder links. In *2019 IEEE International Conference on Space Optical Systems and Applications (ICSOS)*, pages 1–5, 2019. doi:[10.1109/ICSOS45490.2019.8978969](https://doi.org/10.1109/ICSOS45490.2019.8978969).
- [5] Vincent Billault, Jerome Bourderionnet, Jean Paul Mazellier, Luc Leviandier, Patrick Feneyrou, Anaelle Maho, Michel Sotom, Xavier Normandin, Herve Lonjaret, and Arnaud Brignon. Free space optical communication receiver based on a spatial demultiplexer and a photonic integrated coherent combining circuit. *Optics Express*, 29(21):33134–33143, Oct 2021. doi:[10.1364/OE.433087](https://doi.org/10.1364/OE.433087).

- [6] Lorenzo de Marinis, Peter Seigo Kincaid, Yann Lucas, Lea Krafft, Vincent Michau, Matteo Cherchi, Mikko Karppinen, and Giampiero Contestabile. A silicon photonic 32-input coherent combiner for turbulence mitigation in free space optics links. *IEEE Access*, 13:31718–31728, 2025. doi:10.1109/ACCESS.2025.3541870.
- [7] Vincent Billault, Luc Leviandier, Jérôme Bourderionnet, Christophe Pierre, Raynald Sanquer, Marc Castaing, and Arnaud Brignon. Evaluation of a photonic lantern spatial demultiplexer-based receiver for optical communication. *Optics Letters*, 50(5):1512–1515, Mar 2025. doi:10.1364/OL.542129.
- [8] Barnaby Norris and Joss Bland-Hawthorn. Astrophotonics: The rise of integrated photonics in astronomy. *Optics and Photonics News*, 30(5):26–33, 2019.
- [9] T. A. Birks, I. Gris-Sánchez, S. Yerolatsitis, S. G. Leon-Saval, and R. R. Thomson. The photonic lantern. *Advances in Optics and Photonics*, 7(2):107–167, Jun 2015. doi:10.1364/AOP.7.000107.
- [10] S Gross and MJ Withford. Ultrafast-laser-inscribed 3d integrated photonics: challenges and emerging applications. *Nanophotonics*, 4(3):332–352, 2015.
- [11] Jean-François Morizur, Lachlan Nicholls, Pu Jian, Seiji Armstrong, Nicolas Treps, Boris Hage, Magnus Hsu, Warwick Bowen, Jiri Janousek, and Hans-A. Bachor. Programmable unitary spatial mode manipulation. *J. Opt. Soc. Am. A*, 27(11):2524–2531, Nov 2010. doi:10.1364/JOSAA.27.002524.
- [12] Yuanhang Zhang and Nicolas K Fontaine. Multi-plane light conversion: a practical tutorial, 2023. arXiv:2304.11323, doi:10.48550/arXiv.2304.11323.
- [13] José C. A. Rocha, Unè G. Bütaitè, Joel Carpenter, and David B. Phillips. Self-configuring high-speed multi-plane light conversion. *Nature Communications*, 17(1):73, Dec 2025. doi:10.1038/s41467-025-66798-2.
- [14] J. R. Fienup. Phase-retrieval algorithms for a complicated optical system. *Applied Optics*, 32(10):1737–1746, Apr 1993. doi:10.1364/AO.32.001737.
- [15] Haiyan Wang and Rafael Piestun. Dynamic 2d implementation of 3d diffractive optics. *Optica*, 5(10):1220–1228, Oct 2018. doi:10.1364/OPTICA.5.001220.
- [16] Xing Lin, Yair Rivenson, Nezh T. Yardimci, Muhammed Veli, Yi Luo, Mona Jarrahi, and Aydogan Ozcan. All-optical machine learning using diffractive deep neural networks. *Science*, 361(6406):1004–1008, 2018. doi:10.1126/science.aat8084.
- [17] Deniz Mengu, Yi Luo, Yair Rivenson, and Aydogan Ozcan. Analysis of diffractive optical neural networks and their integration with electronic neural networks. *IEEE Journal of Selected Topics in Quantum Electronics*, 26(1):1–14, 2020. doi:10.1109/JSTQE.2019.2921376.
- [18] Tiankuang Zhou, Xing Lin, Jiamin Wu, Yitong Chen, Hao Xie, Yipeng Li, Jingtao Fan, Huaqiang Wu, Lu Fang, and Qionghai Dai. Large-scale neuromorphic optoelectronic computing with a reconfigurable diffractive processing unit. *Nature Photonics*, 15(5):367–373, May 2021. doi:10.1038/s41566-021-00796-w.
- [19] Mustafa Yildirim, Niyazi Ulas Dinc, Ilker Oguz, Demetri Psaltis, and Christophe Moser. Nonlinear processing with linear optics. *Nature Photonics*, 18(10):1076–1082, Oct 2024. doi:10.1038/s41566-024-01494-z.
- [20] Peng Jia, Dongmei Cai, Dong Wang, and Alastair Basden. Simulation of atmospheric turbulence phase screen for large telescope and optical interferometer. *Monthly Notices of the Royal Astronomical Society*, 447(4):3467–3474, 01 2015. doi:10.1093/mnras/stu2655.
- [21] Nicolas Barré. Fluxoptics.jl: A differentiable wave optics framework for inverse design in julia. *Journal of Open Source Software*, 11(118):9734, 2026. doi:10.21105/joss.09734.
- [22] Nicolas Barré and Alexander Jesacher. Inverse design of gradient-index volume multimode converters. *Optics Express*, 30(7):10573–10587, Mar 2022. doi:10.1364/OE.450196.
- [23] Nicolas Barré. Beam shaping algorithm with optimization parameters, 2018. arXiv:1802.05329, doi:10.48550/arXiv.1802.05329.